

THE REFRACTIVE INDEX OF GALLIUM ANTIMONIDE

RESEARCH ARTICLE

Ulrich Galander^{*1,2}, Nicolas Huwyler^{3,4}, Mirela Encheva¹, Matthias Golling^{3,5}, and Oliver H. Heckl^{†1}

¹Optical Metrology, Faculty of Physics, University of Vienna, Boltzmanngasse 5, 1090 Vienna, Austria

²Vienna Doctoral School in Physics, University of Vienna, Boltzmanngasse 5, 1090 Vienna, Austria

³ETH Zurich, Department of Physics, Institute for Quantum Electronics, Auguste-Piccard-Hof 1, 8093 Zurich, Switzerland

⁴Université de Neuchâtel, Institut de Physique, Laboratoire Temps-Fréquence, Avenue de Bellevaux 51, 2000 Neuchâtel, Switzerland

⁵RhySearch, Optical Coating & Characterization Lab, Werdenbergstrasse 4, 9471 Buchs, Switzerland

February 16, 2026

ABSTRACT

Gallium antimonide (GaSb) is a key material for near- and mid-infrared photonics, enabling high-performance laser architectures and detectors. Design and simulation of such devices depend on accurate optical material data, especially the complex refractive index $n_{\text{GaSb}}^* = n_{\text{GaSb}} + ik_{\text{GaSb}}$, consisting of the real part n_{GaSb} (refractive index) and the imaginary part k_{GaSb} (extinction coefficient). However, GaSb refractive index values are based either on theoretical models, typically informed by legacy experimental data, or on experimental measurements without quantified uncertainties. This limits their reliability for state-of-the-art devices. Here, we present measurement results of n_{GaSb}^* in the near- to mid-infrared range from $1\text{ }\mu\text{m}$ to $3.1\text{ }\mu\text{m}$ with a relative uncertainty $<7.8 \times 10^{-5}$ for n_{GaSb} , and $<2.0 \times 10^{-3}$ for k_{GaSb} . As a side result of our method, we also report n_{AlAsSb} for aluminium arsenide antimonide ($\text{AlAs}_{0.08}\text{Sb}_{0.92}$) with a relative uncertainty $<3.9 \times 10^{-4}$. Our results are based on two complementary measurements on a GaSb/AlAsSb-based heteroepitaxial structure under controlled environmental conditions: photometric transmission and layer-thickness analysis by cross-sectional scanning electron microscopy. We simultaneously retrieve the refractive indices of the two materials by fitting a Sellmeier equation and a theoretical dispersion model by Djurišić *et al.* [1]. The uncertainties of n_{GaSb}^* and n_{AlAsSb} are quantified using a Monte Carlo-based approach. Our results provide accurate complex refractive index values for GaSb, which are vital to advance photonics-related technologies in the near- and mid infrared spectral region.

Keywords refractive index · semiconductor · gallium antimonide · optical metrology

1 Introduction

Semiconductors fundamentally changed modern technology through their widespread use in applications such as solar cells, diodes, and transistors in integrated circuits, thus making them a crucial component in many electronic devices. Consequently, a thorough understanding of their properties is essential to enable further technological advances in these areas.

Among semiconductors, GaSb is of particular interest because of its narrow band gap of $\approx 0.72\text{ eV}$ ($\approx 1.7\text{ }\mu\text{m}$), which makes it suitable for a variety of applications. For example, GaSb is used in thermophotovoltaic cells, demonstrating high efficiencies [2], and Huang *et al.* [3] developed an InAs/GaSb semiconductor-based type-II superlattice for imaging in the near-infrared (NIR) ($1.7\text{ }\mu\text{m}$ to $3\text{ }\mu\text{m}$) and mid-infrared (MIR) ($3\text{ }\mu\text{m}$ to $5\text{ }\mu\text{m}$) spectral regions. Furthermore, GaSb-based heteroepitaxial structures are essential for active optoelectrical devices operating in the molecular fingerprint region. Examples include vertical-cavity surface-emitting lasers (VCSELs) [4], superluminescent diodes [5],

^{*}ulrich.galander@univie.ac.at

[†]oliver.heckl@univie.ac.at

quantum cascade lasers (QCLs) [6, 7], and vertical external-cavity surface-emitting lasers (VECSELs) [8], as well as passive elements like the semiconductor saturable absorber mirror (SESAM) [9, 10].

To advance the development of these applications, precise knowledge of the optical properties of GaSb is vital. Among these optical properties, the complex refractive index n^* is fundamental because it governs light propagation and light-matter interaction. For GaSb, several experimental [11–15] and theoretical studies [1, 16–18] have determined n^* . Typically, theoretical studies derive parameter-based models for the electric permittivity (connected to the complex refractive index via Eq. 2) and use published experimental data to evaluate the parameters, whereas experimental studies primarily use spectroscopic ellipsometry (SE) to obtain the refractive index due to its non-destructive measurement approach and ability to perform *in situ* measurements during thin-film growth. However, these studies have certain shortcomings: (i) Most theoretical models rely either on the experimental datasets from Aspnes *et al.* [11], which cover photon energies from 1.5 eV to 6 eV ($\approx 0.206 \mu\text{m}$ to $0.826 \mu\text{m}$), or on data from Ferrini *et al.* [13], which include the GaSb bandgap region as well, making these two datasets the main experimental sources. (ii) The experimental studies investigate different sample types but report only limited sample details, making meaningful comparisons difficult. For example, Aspnes *et al.* [11] measured p-doped ($1.5 \times 10^{17} \text{ cm}^{-3}$) bulk GaSb oriented along the $\langle 111 \rangle$ crystal axis; Ferrini *et al.* [13] measured a molecular beam epitaxy (MBE) grown single layer of GaSb without reporting the doping concentration; and Uribe *et al.* [12] reported the doping concentration but did not mention the growth method. (iii) Most experimental studies rely on SE to determine the refractive index, and SE comes with its own limitations. SE measures polarization changes upon reflection of a sample, typically thin-films on a substrate. As a consequence, samples with depolarization effects such as a rough surface or a non-uniform layer thickness, introduce errors. SE also requires an extensive data analysis, offers low spatial resolution, and has difficulties determining low absorption coefficients ($\alpha < 100 \text{ cm}^{-1}$, with $\alpha \propto k$) [19]. Moreover, the layer thickness is extracted indirectly from optical interference within the thin-film in a transparent wavelength region, hence it is inherently dependent on the optical measurement. (iv) Most studies do not report uncertainty estimates for their results, therefore a quantitative assessment and comparison are not possible, which makes the reported values unsuitable for device design.

In this study, we present an alternative approach to refractive index measurements based on Perner *et al.* [20], that addresses the shortcomings above. We provide a complete description of sample preparation and avoid SE specific drawbacks, such as the indirect measurement of the layer thicknesses. Consequently, we give a quantitative uncertainty analysis of our results. Specifically, we measure the photometric transmission of a GaSb/AlAsSb heteroepitaxial structure and determine the individual layer thicknesses using a scanning electron microscope (SEM), in this way avoiding the indirect method used in SE. We then perform a nonlinear regression based on our measurements to fit a parameterized refractive index model for n_{GaSb}^* and a Sellmeier equation for n_{AlAsSb} . Finally, we quantify our results with a Monte Carlo-based uncertainty estimation.

2 Theoretical Background

The electric permittivity of any material is given by

$$\epsilon(E) = \epsilon_1(E) + i\epsilon_2(E), \quad (1)$$

where $\epsilon_1(E)$ is the real part, $\epsilon_2(E)$ is the imaginary part of $\epsilon(E)$, and E is the photon energy. The refractive index $n^*(E)$ of the material is related to $\epsilon(E)$ via

$$n^*(E) = \sqrt{\epsilon(E)}. \quad (2)$$

This implies that $n^*(E) \in \mathbb{C}$, with

$$n^*(E) = n(E) + ik(E), \quad (3)$$

where $n(E)$ represents the real refractive index and $k(E)$ the extinction coefficient. From Eqs. 1–3 we derive that $n(E)$ and $k(E)$ are functions of $\epsilon_1(E)$ and $\epsilon_2(E)$

$$n(E) = \sqrt{\frac{\sqrt{\epsilon_1^2(E) + \epsilon_2^2(E)} + \epsilon_1(E)}{2}}, \quad (4)$$

$$k(E) = \sqrt{\frac{\sqrt{\epsilon_1^2(E) + \epsilon_2^2(E)} - \epsilon_1(E)}{2}}. \quad (5)$$

Thus, knowing $\epsilon(E)$, one can deduce the refractive index and extinction coefficient.

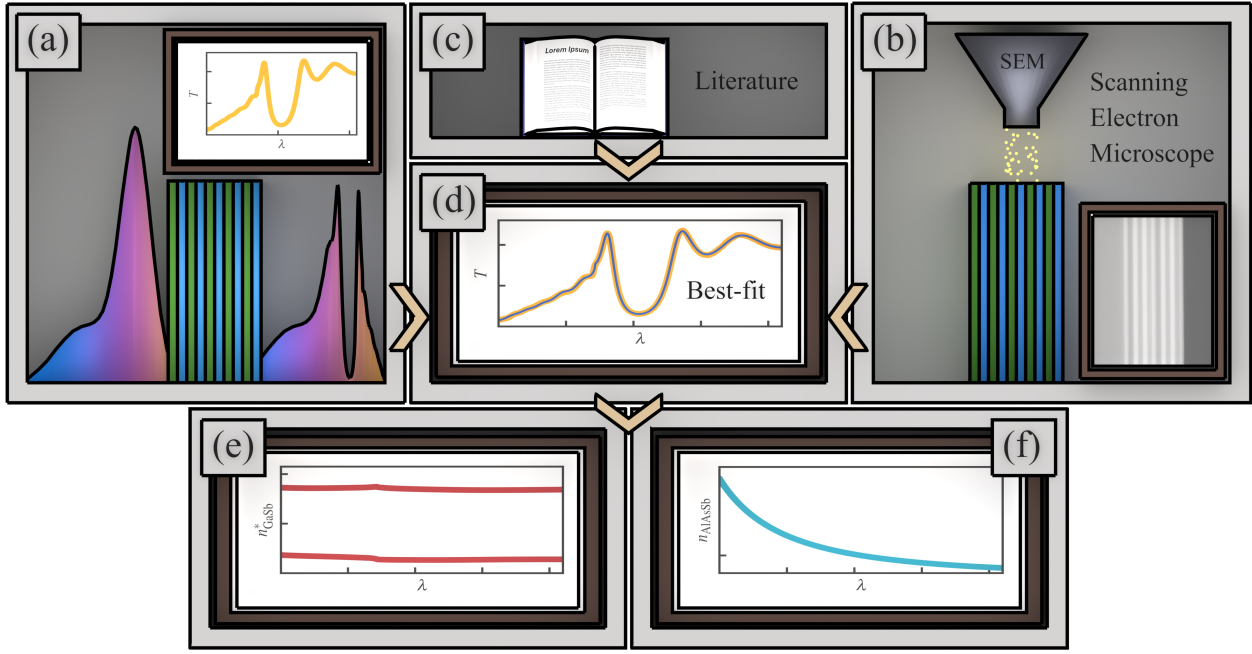


Fig. 1: Overview of the workflow. (a) We measure the photometric transmission T and (b) record cross-sectional images of the structure to extract the layer thicknesses $\{d_i\}$. (c) With literature values for n_{Sub} , we (d) perform a nonlinear fit of a theoretical model for n_{GaSb}^* and the Sellmeier coefficients of n_{AlAsSb} to T with $\{d_i\}$ as additional input. We use the fit parameters to calculate (e) n_{GaSb}^* and (f) n_{AlAsSb} .

3 Methods

Fig. 1 illustrates our approach to determine n_{GaSb}^* and n_{AlAsSb} . As shown in Fig. 1(a), we first measure the photometric transmission T and subsequently, determine the layer thicknesses $\{d_i\}$ from cross-sectional images of the heteroepitaxial structure (Fig. 1(b)). We then fit a theoretical model for the complex refractive index of GaSb (n_{GaSb}^*) and a Sellmeier equation for the refractive index of AlAsSb (n_{AlAsSb}) to T (Fig. 1(d)), using the measured $\{d_i\}$ as additional input. For the refractive index of the substrate (n_{Sub}), we use literature values (Fig. 1(c)). Finally, we determine n_{GaSb}^* and n_{AlAsSb} from the fit parameters (Fig. 1(e) and (f)).

The measurements of T and the cross-sectional images (Fig. 1(a) and (b)) are described in detail in Sec. 3.3 and 3.4, respectively. The determination of $\{d_i\}$ is described in Sec. 3.5.

To perform a nonlinear fit to T (Fig. 1(d)), we first require a mathematical framework. The dependence of T on n_{GaSb}^* , n_{AlAsSb} , and n_{Sub} is fully governed by the Fresnel's equations and the respective layer thicknesses $\{d_i\}$. Thus, we model T using the transfer-matrix method (TMM)

$$T = \text{TMM}(n_{\text{GaSb}}^*, n_{\text{AlAsSb}}, \{d_i\}, n_{\text{Sub}}). \quad (6)$$

This equation also highlights the importance of independently measuring $\{d_i\}$. The quantity n_{GaSb}^* can be written as a function of the photon energy E and the material-specific parameters, (the fit parameters $\vec{\theta}$), as

$$n_{\text{GaSb}}^* = n_{\text{GaSb}}^*(E, \vec{\theta}). \quad (7)$$

The full theoretical model for n_{GaSb}^* is explained in detail in Sec. 3.1. The refractive index n_{AlAsSb} is described by a Sellmeier equation¹

$$n_{\text{AlAsSb}}^2 - 1 = \frac{B\lambda^2}{\lambda^2 - B_0} + \frac{C\lambda^2}{\lambda^2 - C_0}, \quad (8)$$

with λ denoting the wavelength and B , B_0 , C , and C_0 being Sellmeier coefficients. The value of n_{Sub} is taken from Aspnes *et al.* [21]. We can now rewrite Eq. 6 as

$$T = \text{TMM}(E, \vec{\theta}, B, B_0, C, C_0, \{d_i\}, n_{\text{Sub}}), \quad (9)$$

¹The Sellmeier equation is based on unpublished experimental measurements communicated privately by Dr. V. J. Wittwer from the Université de Neuchâtel.

showing the explicit dependence of the model parameters and Sellmeier coefficients. Fig. 1(d) shows the nonlinear fit procedure and highlights the various input parameters. We fit Eq. 9 to the measured T , using the measured $\{d_i\}$ as additional inputs, and extract the model parameters $\vec{\theta}$ and the Sellmeier coefficients. The full fit procedure is described in Sec. 3.6. In the last step, depicted in Fig. 1(e) and (f), we use these fitted parameters to simultaneously calculate n_{GaSb}^* and n_{AlAsSb} .

3.1 Refractive Index Model for GaSb

To fit Eq. 9 we need a theoretical model for n_{GaSb}^* . For GaSb, several different such models exist. However, most of them are either too intricate to be used in a fit procedure (see Ref. [17, 18, 22]) or are inaccurate in their description (see Ref. [16]). We use the model of Djurišić *et al.* [1] because it yields good results, offers a comprehensive description, and is straightforward to implement.

The following section is based on the work of Djurišić *et al.* [1]. For a detailed discussion of the individual equations and parameters, we refer to the original literature. Here, we present only the formulas used.

The authors separate the electric permittivity into a sum of its constituents,

$$\epsilon(E) = \epsilon_{1\infty} + \epsilon_{\text{I}}(E) + \epsilon_{\text{II}}(E) + \epsilon_{\text{III}}(E), \quad (10)$$

where each contribution corresponds to different critical points (CPs) within the material's Brillouin zone. In total, the model of Djurišić *et al.* has 24 parameters.

$\epsilon_{1\infty}$: $\epsilon_{1\infty}$ is a constant describing CP transitions outside the investigated spectral range [1].

$\epsilon_{\text{I}}(E)$: The E_0 and $E_0 + \Delta_0$ CPs are described by

$$\epsilon_{\text{I}}(E) = AE_0^{-3/2} \left[f(\chi_0) + \frac{1}{2} \left(\frac{E_0}{E_0 + \Delta_0} \right)^{3/2} f(\chi_{0s}) \right], \quad (11)$$

where A is the strength parameter for this transition and $f(\chi_0)$ and $f(\chi_{0s})$ are given by

$$f(y) = y^{-2} \left[2 - (1+y)^{1/2} - (1-y)^{1/2} \right]. \quad (12)$$

χ_0 and χ_{0s} are defined via

$$\chi_n = \frac{E + i\Gamma_n}{E_n}, \quad \chi_{ns} = \frac{E + i\Gamma_n}{E_n + \Delta_n}, \quad (13)$$

with $n = 0$. Γ_0 is the damping parameter for the E_0 and $E_0 + \Delta_0$ transition.

$\epsilon_{\text{II}}(E)$: The E_1 and $E_1 + \Delta_1$ CP transitions are expressed through

$$\epsilon_{\text{II}} = -B_1 \chi_1^{-2} \ln(1 - \chi_1^2) - B_{1s} \chi_{1s}^{-2} \ln(1 - \chi_{1s}^2), \quad (14)$$

where χ_1 and χ_{1s} are obtained by Eq. 13 with $n = 1$. B_1 and B_{1s} are strength parameters for this transition and Γ_1 is the damping coefficient.

$\epsilon_{\text{III}}(E)$: Higher lying CP transitions are modeled by damped harmonic oscillators

$$\epsilon_{\text{III}} = \sum_{j=2}^4 \frac{F_j^2}{E_j^2 - E^2 - iE\Gamma_j} \quad (15)$$

with strength $F_j = \sqrt{f_j E_j^2}$.

For each transition, the authors introduce a frequency-dependent damping function

$$\Gamma_j(E) = \Gamma_j \exp \left[-\alpha_j \left(\frac{E - E_j}{\Gamma_j} \right)^2 \right], \quad (16)$$

where Γ_j are damping constants, E_j are transition energies, and E is the photon energy. α_j are parameters to continuously change the lineshapes. According to the authors, Eq. 16 is the main driver for improvements in accuracy compared to other models.

The complex refractive index $n^*(E)$ is computed via Eq. 2.

3.2 Sample Preparation

The sample characterized in this work is based on an epitaxial heterostructure designed as a distributed Bragg reflector (DBR) for a center wavelength of $2.05\text{ }\mu\text{m}$. We grow the epitaxial heterostructure using a Veeco Gen III research MBE reactor. The growth is performed on a tellurium-doped, $500\text{ }\mu\text{m}$ -thick, 2-inch single-side polished GaSb substrate supplied by Wafer Technology Ltd. The layer sequence starts by depositing a 250 nm thick $\text{InAs}_{0.91}\text{Sb}_{0.09}$ layer that serves as an etch-stop to facilitate subsequent substrate removal. This layer is then capped by the 6.5-period $\text{GaSb}/\text{AlAs}_{0.08}\text{Sb}_{0.92}$ DBR. The resulting heteroepitaxial structure has a total thickness of $2.14\text{ }\mu\text{m}$, with the DBR investigated in this work constituting $1.9\text{ }\mu\text{m}$. Further details regarding the growth parameters can be found in [23].

Following growth, the wafer is cleaved into $1.5 \times 1.5\text{ cm}^2$ samples. Larger ($1.6 \times 1.6\text{ cm}^2$) double-side polished, undoped GaAs pieces are prepared for use as bonding carriers. GaAs is chosen for the bonding carriers due to its transparency above 808 nm . Both, the samples and carrier pieces, underwent a solvent cleaning procedure (methanol, isopropyl alcohol, and acetone) as described in Ref. [24], followed by surface activation via oxygen plasma (Technics Plasma 100-E). Direct wafer bonding is subsequently performed in a wafer bonder (Applied Microengineering Ltd), applying a force of 1000 N at $300\text{ }^\circ\text{C}$. The GaSb substrate is then removed in a two-stage process. First, the majority of the GaSb substrate is mechanically thinned by lapping to a residual thickness of $\approx 20\text{ }\mu\text{m}$. Second, the remaining GaSb substrate is chemically removed using a $\text{CrO}_3 : \text{HF} : \text{H}_2\text{O}$ wet-etching solution. Finally, the etch-stop layer is selectively removed using a citric acid and hydrogen peroxide solution. A comprehensive description of this fabrication workflow is available in Refs. [23–25].

3.3 Transmission Measurement

We measure the photometric transmission of the sample with a Varian Cary 5 UV-Vis-NIR spectrophotometer at normal incidence. The spectrophotometer covers a wavelength range of $0.175\text{ }\mu\text{m}$ to $3.3\text{ }\mu\text{m}$ with an accuracy of $\pm 0.1\text{ nm}$ in the UV-Vis spectral range and $\pm 0.4\text{ nm}$ in the NIR spectral range. During the measurements, the Cary 5 operates in double beam mode and records spectra in the wavelength range from $0.9\text{ }\mu\text{m}$ to $3.3\text{ }\mu\text{m}$. We measure at a scan rate of 600 nm min^{-1} with a resolution of 1 nm , and an average time of 0.1 s . During this 0.1 s period, the Cary 5 averages three measured data points. To account for this, we apply a scaling factor of $3^{-1/2}$ to the 1σ standard uncertainty of the mean ($s(T)$). We set the beam size with a 7.5 mm precision pinhole (Thorlabs, P7500K) mounted to a custom made sample holder and measure three different types of spectra:

- (i) 0% transmission spectrum ($T_{0\%}$), where the light path is blocked and we measure the dark counts of the detector.
- (ii) 100% transmission spectrum ($T_{100\%}$), where we measure the full throughput without the sample.
- (iii) Sample transmission spectrum (T_{sample}), where the sample is placed in the light path of the Cary 5.

The background spectra ($T_{0\%}$ and $T_{100\%}$) are measured ten times and T_{sample} is measured 100 times. We calculate the average of each spectrum type and apply the baseline correction formula

$$T = \frac{T_{\text{sample}} - T_{0\%}}{T_{100\%} - T_{0\%}}, \quad (17)$$

to the averages to obtain the background corrected photometric transmission spectra of our sample (T). We propagate $s(T)$ through Eq. 17 using the `uncertainties` package for Python 3 [26]. Fig. 2(a) shows T , while Fig. 2(b) presents $s(T)$. Due to high detector noise at longer wavelengths ($>3.1\text{ }\mu\text{m}$) and high absorption of GaSb at shorter wavelengths ($<1\text{ }\mu\text{m}$), we restrict our data to the $1\text{ }\mu\text{m}$ to $3.1\text{ }\mu\text{m}$ spectral range. The entire measurement run ($\sim 9\text{ h}$) is conducted in a climate-controlled laboratory, with the temperature maintained at $20.4(5)\text{ }^\circ\text{C}$. Water vapor absorption lines are removed during the baseline correction (Eq. 17).

3.4 Cross-Section Measurement

We conduct the cross-sectional measurements using a SEM (Zeiss Supra 55 VP) equipped with a four-quadrant backscattered electron detector. Before starting the measurements, we evacuate the SEM to a pressure of approximately $2 \times 10^{-6}\text{ mbar}$, set the working distance to 9.4 mm , and the beam energy to 10 keV . Afterwards, we acquire calibration images at 30 kX and 50 kX magnification using a NIST-certified calibration standard (EM-TEC MCS-0.1CF). We then record cross-sectional images of our sample. At each position, we take images at both 30 kX (Fig. 3(a)) and 50 kX (Fig. 3(b)) magnification. Fig. 3(c) and 3(d) show the column-wise calculated mean line profile (green line), with the orange and blue stripes marking the extracted layer thicknesses.

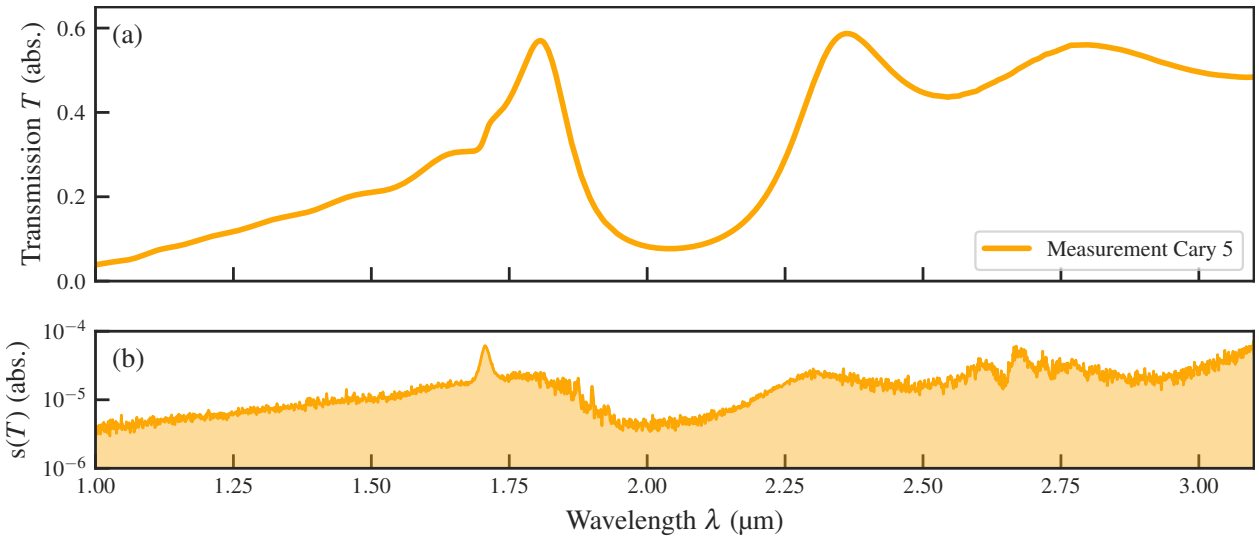


Fig. 2: (a) The baseline-corrected transmission of the heteroepitaxial sample, measured using a Varian Cary 5 in the wavelength range from $1\text{ }\mu\text{m}$ to $3.1\text{ }\mu\text{m}$. (b) 1σ standard uncertainty of the mean measurement shown in panel (a).

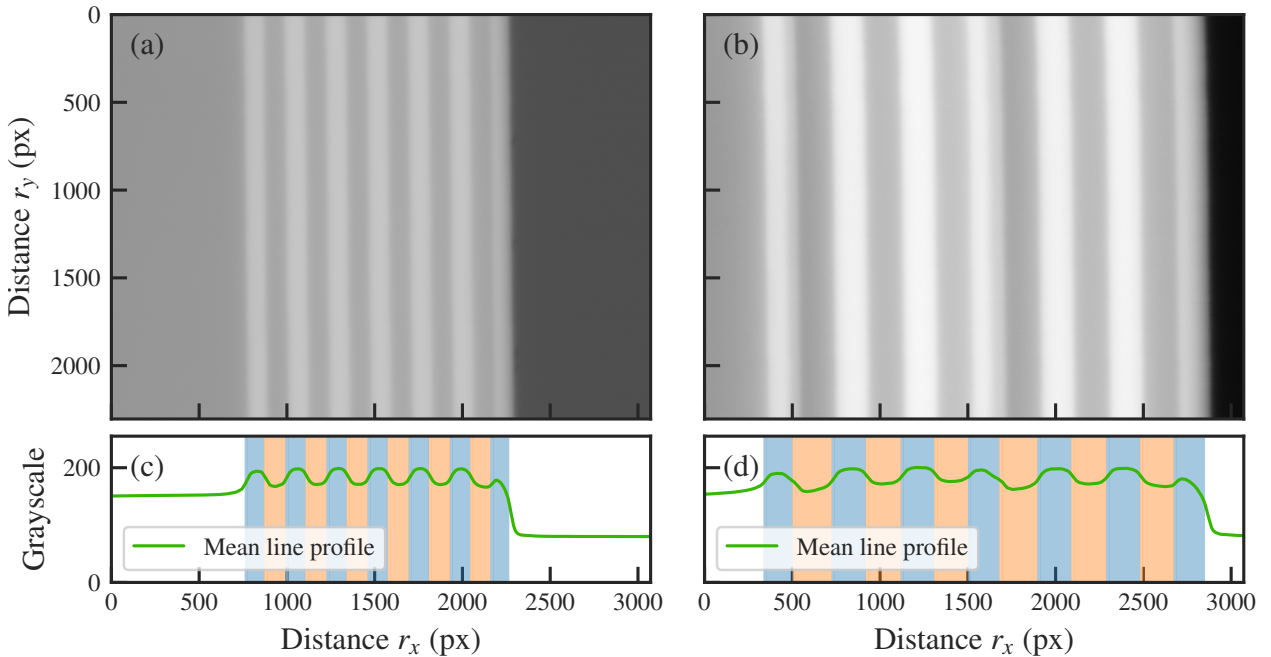


Fig. 3: Representative cross-sectional grayscale image of the sample with (a) 30 kX and (b) 50 kX magnification, respectively. The green line shows the column-wise mean grayscale intensity for (c) 30 kX and (d) 50 kX magnification. The orange and blue stripes indicate the extracted layer thicknesses.

3.5 Layer Thickness Extraction

To extract the layer thicknesses from the recorded grayscale images (see Fig. 3), we use a custom Python 3 program, similar to that described in Ref. [20]. First, we apply the program to the images of the calibration standard (see Sec. 3.4) and determine a calibrated pixel pitch of $1.236\ 22(7)\text{ nm px}^{-1}$ at 30 kX magnification and $0.742\ 67(6)\text{ nm px}^{-1}$ at 50 kX magnification, respectively. These calibration values are later used in **Step 5** to convert the layer thickness from pixels into a physical distance in μm .

The program's workflow is described below:

Step 1: Load the image into a 2D array. We notice that the images have blank lines at the top and the bottom, hence we consider only rows r_y from 100 to 2200 and columns r_x from 10 to 3000.

Step 2: Compute the column-wise mean intensity to obtain the average line profile (green line in Fig. 3(c),(d)). Differentiate this line profile and take the position of its local extrema as estimates for the interface position between neighboring layers.

Step 3: Loop over all rows in the 2D array:

- (i) Split the row into symmetric intervals around the previously estimated interfaces, ensuring that each interval contains exactly one interface.
- (ii) Fit an error function to each interval. The gradual intensity transition observed at the layer interfaces is accurately modeled by an error function, where the inflection point of the fitted curve estimates the location of the interface.
- (iii) The difference between adjacent inflection points corresponds to the layer thickness in pixels.

Step 4: Calculate the mean and 1σ standard uncertainty of the mean $s(d_i)$ for each extracted layer thickness d_i of the sample.

Step 5: Multiply by the calibrated pixel pitch to convert $\{d_i\}$ into physical distances in μm .

Step 6: Combine the mean values and 1σ standard uncertainty of the mean $s(\{d_i\})$ of both magnifications. We use a weighted average to account for the different $s(\{d_i\})$.

The extracted mean layer thicknesses $\{d_i\}$ are displayed in Fig. 4(a). The corresponding 1σ standard uncertainty $s(\{d_i\})$ is shown in Fig. 4(b).

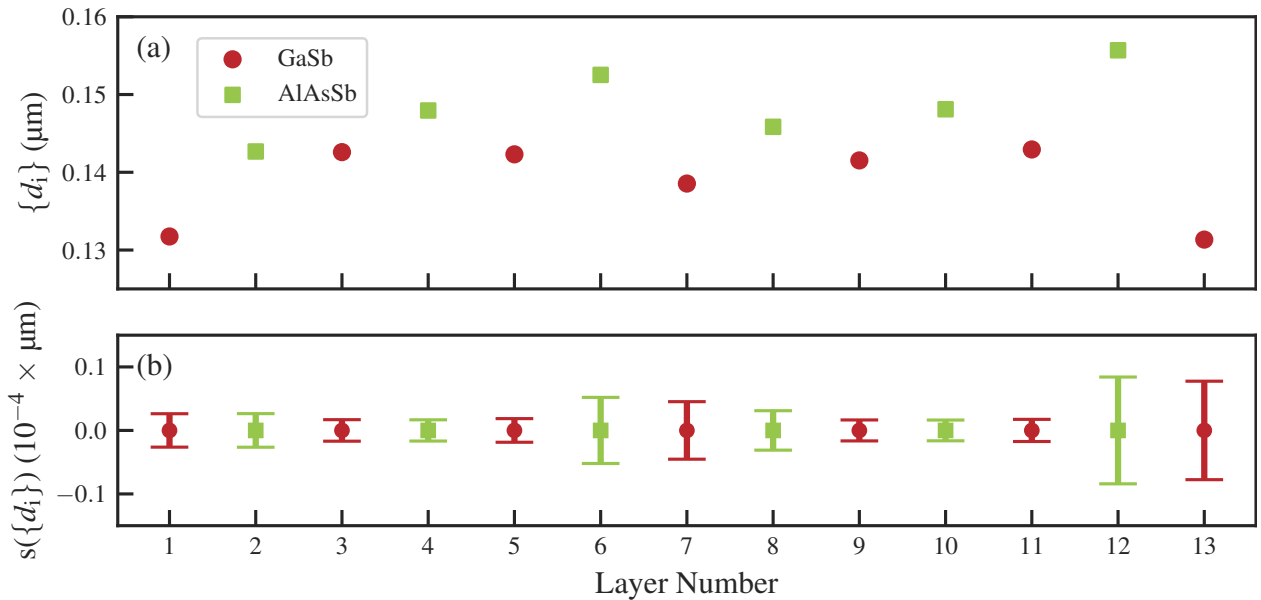


Fig. 4: (a) The extracted physical layer thicknesses $\{d_i\}$. Red circles corresponds to GaSb and green squares to AlAsSb, respectively. (b) The 1σ standard uncertainty $s(\{d_i\})$ of the individual layer thicknesses. Note the scaling factor 10^{-4} in front.

3.6 Nonlinear Fit Procedure

The fitting framework is built on the Python 3 library `lmfit` [27] and the best fit is found by minimizing the residuals r_i

$$r_i = T - T_{\text{model}}, \quad (18)$$

where T is described in Sec. 3.3 and T_{model} denotes the simulated transmission calculated using the `tmm-fast` library for Python 3 [28]. To perform this minimization, the Log-Cosh Loss objective function $L(r_i)$

$$L(r_i) = \sum_{i=1}^n \log(\cosh(r_i)), \quad (19)$$

is used since it is smooth (unlike the mean absolute error), less sensitive to outliers than the mean squared error, and does not need an additional parameter such as the Huber loss [29].

As mentioned in Sec. 3 (see also Fig. 1(d)), we fit Eq. 9, with the measured layer thicknesses $\{d_i\}$ as input, to the photometric transmission T . The fit parameters correspond to the Sellmeier coefficients and the model parameters $\vec{\theta}$ as described in Sec. 3 and 3.1.

The nonlinear fit procedure is structured as follows: (i) we first identify parameters (that are Sellmeier coefficients and $\vec{\theta}$) by finding a global optimum using a single run of a time-expensive global optimizer, (ii) we refine these found parameters with a fast local optimizer. We use this approach, because initial parameters are crucial for finding optimal solutions for our non-convex objective function, and this way we can start the second optimization within a convex region near the global optimum. The global optimizer we use is Adaptive Memory Programming for Constrained Global Optimization (AMPGO) [30] and the local optimizer is Nelder-Mead simplex algorithm [31, 32].

The fit result is presented in Fig. 5(a) (blue line). The relative root mean square error (RRMSE) is 0.75 %, suggesting strong agreement between measurement and fit. This is especially evident from the residuals depicted in Fig. 5(b). The sharp edge at $\approx 1.7 \mu\text{m}$ is inherent to the refractive index model of GaSb and can be traced back to Eq. 12, in particular the term $\sqrt{1 - y}$, where y is a complex number.

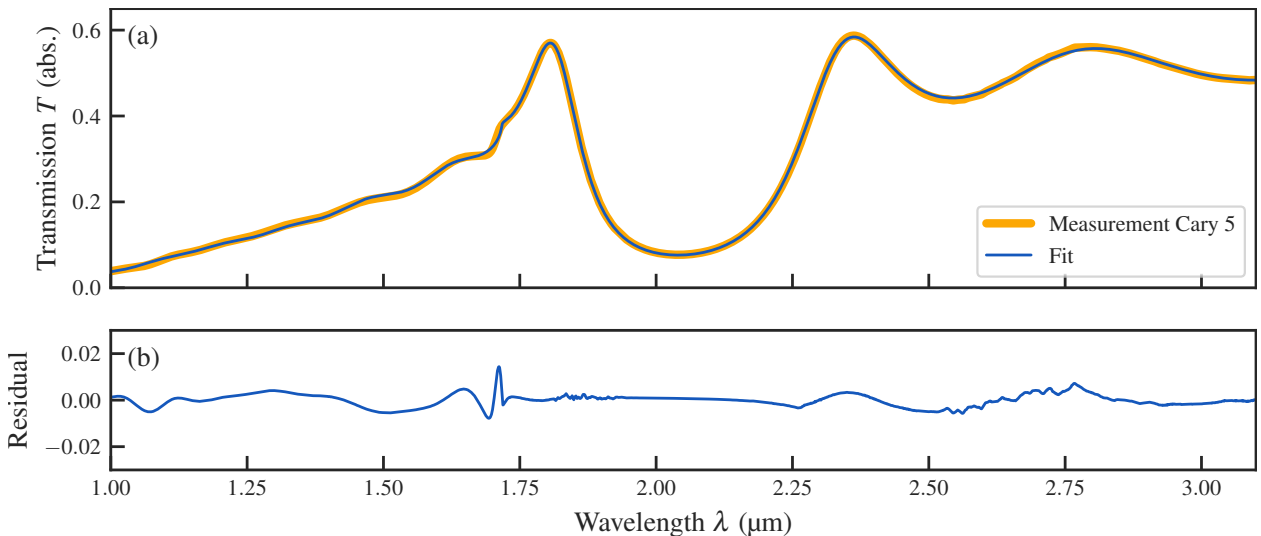


Fig. 5: (a) The measured photometric transmission T (thick yellow line) together with the best-fit result (thin blue line). (b) The corresponding residual, obtained via Eq. 18.

3.7 Uncertainty Estimation

The uncertainties in n_{GaSb}^* and n_{AlAsSb} are evaluated using Eq. 9. However, a straightforward analytical uncertainty propagation is not available because TMM is an intricate function and the model parameters are obtained via a nonlinear fit [20]. Consequently, we employ a numerical (Monte Carlo) approach to propagate the uncertainties, following Ref. [20], which allow us to propagate the known uncertainties of the experimental inputs through the fitting procedure.

The quantities in Eq. 6 that carry uncertainties are the measured layer thicknesses $\{d_i\}$, the measured transmission T , and the refractive index of the substrate n_{Sub} . To account for these uncertainties, we execute the nonlinear fit procedure 500 times (only the fast local optimizer), each time with a different realization of said quantities. Each fit yields distinct Sellmeier coefficients and model parameters $\vec{\theta}$, as a result giving different values for n_{GaSb}^* and n_{AlAsSb} . Finally, we determine the 1σ standard uncertainty of the mean for n_{GaSb}^* and n_{AlAsSb} , which represents the uncertainty in the measured refractive indices.

We achieve the variation in T , $\{d_i\}$, and n_{Sub} with a resampling approach. For that, we randomly selected the values from a normal distribution centered at the mean values with corresponding standard deviation. For the values used in T and $\{d_i\}$, see Figs. 2 and 4, respectively. For n_{Sub} , we use an uncertainty of 0.2 %, following Ref.[21].

4 Results and Discussion

The real and imaginary parts of n_{GaSb}^* in the spectral range $1 \mu\text{m}$ to $3.1 \mu\text{m}$ are shown in Fig. 6(a) and (b), respectively, as solid red lines. The fit results of the model parameters $\vec{\theta}$ are summarized in Tab. 1. We compare our data with the results of Ferrini *et al.* [13], which were used to derive the refractive index model employed in this work, and with the most recent values found, reported by Wasiak *et al.* [15].

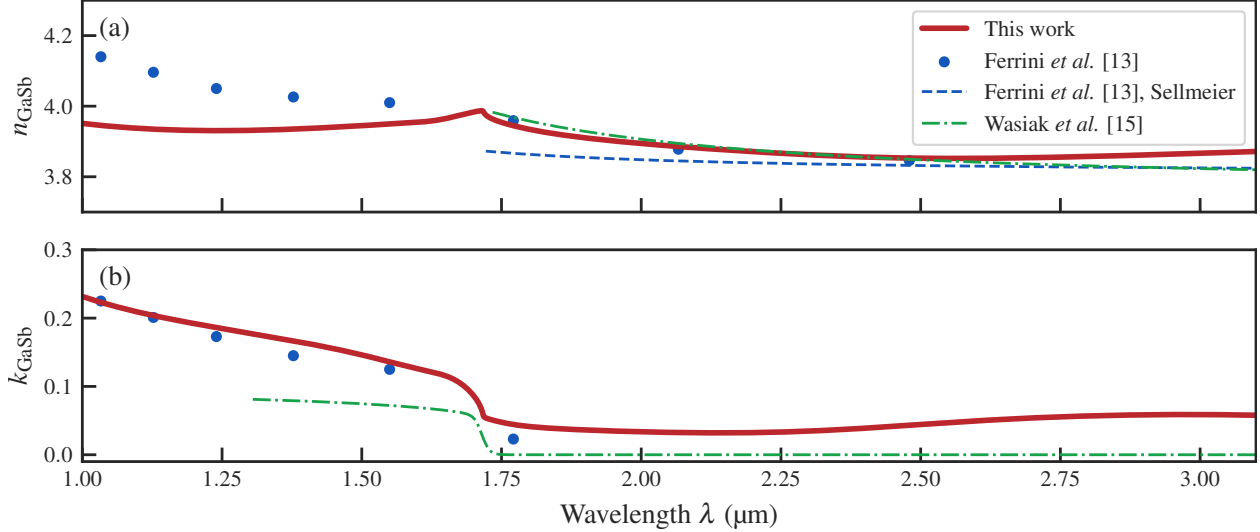


Fig. 6: Our results for n_{GaSb}^* , shown as solid red lines: (a) The real part n_{GaSb} , (b) the imaginary part k_{GaSb} . For comparison, we include experimental values from Ref. [13] (blue dots and blue dashed line) and Ref. [15] (green dot-dashed line). Note: Ref.[15] reports a range of values for the A parameter of the dispersion relation. The values shown here correspond to $A = 12.45$.

E_0 (eV)	E_1 (eV)	E_2 (eV)	E_3 (eV)	E_4 (eV)	Δ_0 (eV)	Δ_1 (eV)	$\epsilon_{1\infty}$
0.722	2.862	0.739	0.421	3.797	1.092	0.020	8.427×10^{-7}
Γ_0 (eV)	Γ_1 (eV)	Γ_2 (eV)	Γ_3 (eV)	Γ_4 (eV)	F_2 (eV)	F_3 (eV)	F_4 (eV)
3.213×10^{-4}	0.949	0.053	0.172	0.095	0.067	0.153	4.256
α_0	α_1	α_2	α_3	α_4	A (eV $^{3/2}$)	B_1	B_{1s}
2.463×10^{-4}	0.239	0.933	1.602	0.013	1.488	12.770	1.512×10^{-4}

Tab. 1: Our fit results for the model parameters $\vec{\theta}$ of n_{GaSb}^* . The values are rounded to three decimal points.

Real part of n_{GaSb}^* : The available data shows that all three curves overlap in the $1.75 \mu\text{m}$ to $2.50 \mu\text{m}$ wavelength region. Above $2.50 \mu\text{m}$ Wasiak's results and ours slightly deviate with a maximum of ≈ 0.052 at $3.1 \mu\text{m}$. This deviation arises from the fact that Wasiak used a strictly monotonically decreasing Sellmeier equation over the full reported wavelength range ($\approx 1.73 \mu\text{m}$ to $11.8 \mu\text{m}$). The part of Ferrini's data which are based on a Sellmeier equation (dashed blue line) do not agree with our results, but align, at longer wavelengths, with those of Wasiak. Below $\approx 1.75 \mu\text{m}$, Wasiak provides no data, and our results diverge from Ferrini's (blue dots), which were obtained by methods other than the Sellmeier equation used at longer wavelengths. Our work shows a relatively flat refractive index behaviour in that region, whereas Ferrini's data presents an ascending trend with decreasing wavelength. The reason for this may lie in their methodology: first, they do not directly measure the layer thickness; instead, they infer it from the amplitude and period of interference oscillations in the measured R spectrum. Second, the refractive index in that region was determined from separate measurements (interference fringes, SE, and KK of R). This is also supported by the fact that the different wavelength ranges reported by Ferrini do not connect at the band gap wavelength (blue dots and blue

dashed line). Finally, we note the peak near the GaSb band gap at ≈ 0.72 eV (≈ 1.7 μm), the same characteristic is reported in Refs. [17, 33].

Imaginary part of n_{GaSb}^* : Unlike the real part of the refractive index, no spectral region shows perfect overlap among all three curves. Ferrini's data and ours agree reasonably well across ≈ 1 μm to 1.75 μm , while Wasiak's values are consistently lower. Note, that Wasiak report the absorption coefficient α for 0.28 eV to 0.95 eV (≈ 4.43 μm to 1.3 μm) instead of the extinction coefficient k_{GaSb} . Accordingly, the values for k_{GaSb} in Fig. 6(b) labeled "Wasiak *et al.* [15]" are computed using $k = \frac{c h \alpha}{E^4 \pi}$, with c the speed of light, h Planck's constant. Both datasets, Wasiak's and ours, do capture the steep decrease in k_{GaSb} around 1.75 μm and Wasiak attribute it to the Urbach tail. Wasiak *et al.* reports absorption near 0.4 eV (≈ 3.1 μm), which they attributed to residual absorption of the substrate; in contrast, we observe an increasing trend of k_{GaSb} at longer wavelengths. Ferrini does not report values for k_{GaSb} for wavelengths higher than ≈ 1.75 μm . Below ≈ 1.75 μm , both our data and Ferrini's exhibit an ascending trend, whereas Wasiak's shows minimal or no increase.

In summary, our results for n_{GaSb}^* in the wavelength range from 1 μm to 3.1 μm show deviations from literature values in specific regions, which we attribute to the differing approaches and analysis used in the various works. As noted above, Ferrini *et al.* rely on an indirect measurement of the layer thickness, and connected multiple methods to obtain the refractive index, including a numerical KK transform based on an extrapolated R spectrum. While these calculations are justified, they introduce a larger margin of error, evident from the not ideal continuity between the Sellmeier-based values (Fig. 6(a) dashed blue line) and the points obtained by the other methods (Fig. 6(a) blue dots). By contrast, Wasiak *et al.* determined the layer thickness by SEM. They derived n_{GaSb} by fitting a Sellmeier model to interference fringes in transmission spectra over the entire reported wavelength range, and they report α rather than k_{GaSb} . In our work, we determine the refractive index using a single measurement technique (photometric transmission) across the entire reported wavelength range, measure the layer thicknesses independently of the optical data using SEM, and employ a dedicated theoretical model for n_{GaSb}^* that describes the real and imaginary parts within a single framework.

The result for n_{AlAsSb} is shown in Fig. 7 and the fitted Sellmeier coefficients are summarized in Tab. 2. To the best of our knowledge, broadband values for n_{AlAsSb} with the same mole fraction as in our sample ($x = 0.08$) are not available in the literature.

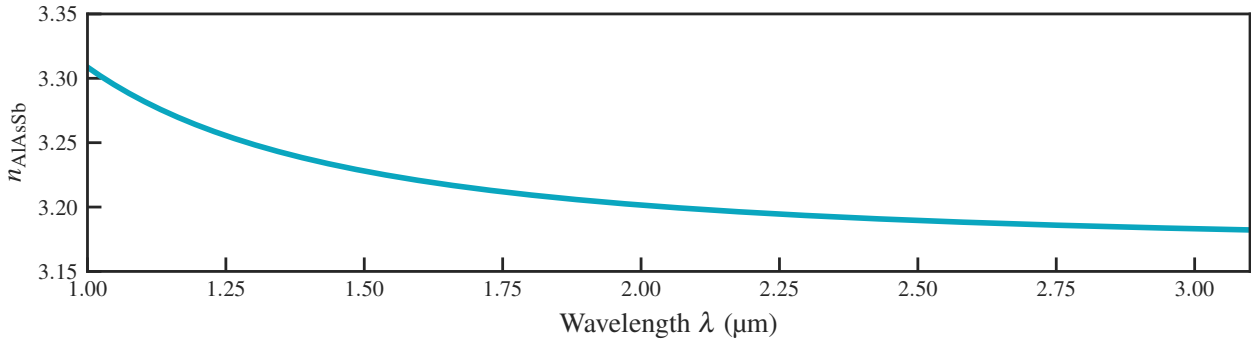


Fig. 7: Our result for the refractive index of $\text{AlAs}_{0.08}\text{Sb}_{0.92}$ using a Sellmeier equation.

B	B_0 (μm^2)	C	C_0 (μm^2)
1.545	0.017	7.496	0.105

Tab. 2: Fitted Sellmeier coefficient (Eq. 8) for AlAsSb, rounded to three decimal points.

The uncertainty estimation described in Sec. 3.7, applied to our results, yield the relative uncertainties presented in Tab. 3.

5 Conclusion

We report complex refractive index values for the III-V semiconductor GaSb and refractive index values for $\text{AlAs}_{0.08}\text{Sb}_{0.92}$, measured in a controlled environment from 1 μm to 3.1 μm . The relative uncertainty are $< 7.8 \times 10^{-5}$

$s(n_{\text{GaSb}})/n_{\text{GaSb}}$	$s(k_{\text{GaSb}})/k_{\text{GaSb}}$	$s(n_{\text{AlAsSb}})/n_{\text{AlAsSb}}$
7.8×10^{-5}	2.0×10^{-3}	3.9×10^{-4}

Tab. 3: Relative uncertainties for $n_{\text{GaSb}}^* = n_{\text{GaSb}} + ik_{\text{GaSb}}$ and n_{AlAsSb} .

for n_{GaSb} , $<2.0 \times 10^{-3}$ for k_{GaSb} , and $<3.9 \times 10^{-4}$ for n_{AlAsSb} . Measurements are performed on a 6.5 period, MBE grown GaSb/AlAsSb thin-film heteroepitaxial structure. Our methodological approach combines measurements of the photometric transmission T with calibrated cross-sectional SEM measurements of the individual layer thicknesses $\{d_i\}$ of the heterostructure. From these measurements, we simultaneously determine n_{GaSb}^* and n_{AlAsSb} by a nonlinear fit procedure. Additionally, we provide an uncertainty estimation based on a Monte Carlo approach to quantify our results. As stated in Ref. [20], this approach can be applied to crystalline or amorphous multilayers and is not limited to DBRs, as it only requires that the sample's optical response shows broadband features unaltered by the spectrometer. Additionally, this method does not rely on specific equipment such as SE [20].

We compare our results with literature values (Refs. [13, 15]) and find deviations in certain wavelength regions, which we attribute to differing methodological approaches. Ref. [13] and Ref. [15] both use a Sellmeier equation for wavelengths longer than $\approx 1.75 \mu\text{m}$, corresponding to the GaSb band gap. However, Sellmeier equations are derived from approximations to the Lorentz oscillator model and are valid only far from resonances [34]. In contrast, we use a dedicated theoretical model (see Sec. 3.1 and Ref. [1]) for n_{GaSb}^* . The layers thickness in Ref. [13] was determined indirectly from interference fringes, which inherently ties the thickness to the optical measurements. In contrast, we measure the thicknesses independently using SEM, thereby decoupling the optical and the thickness measurements. Further, Ref. [13] combines separate measurement approaches to determine n_{GaSb}^* , including interference fringes, SE, and KK calculations of the measured reflection spectrum R , while Ref. [15] and our work employ a single optical measurement technique across the entire reported wavelength range. This highlights the methodological differences among the works and helps explain the discrepancies in the reported results.

Finally, we conclude that our updated complex refractive index data for GaSb will support the design, development, and optimization of future passive and active optoelectronic devices.

Data and Code Availability: The authors can provide data and code upon reasonable request.

Acknowledgment: This research was funded in whole or in part by the Austrian Science Fund (FWF)[10.55776/F1004] and [10.55776/P36040]. For open access purposes, the author has applied a CC BY public copyright license to any author accepted manuscript version arising from this submission. We acknowledge support by Stephan Puchegger and Martin Haßler and the Faculty Center for Nano Structure Research at the University of Vienna. All sample preparation steps were conducted at the FIRST cleanroom facility at ETH Zürich. Instrument identification in this paper is for experimental clarity only and does not imply endorsement.

Author Contribution: U.G.: Writing – original draft (lead), Writing – review and editing (lead), Visualization (lead), Project administration (lead), Data curation (lead), Investigation (lead), Formal analysis (lead), Software (lead). N.H.: Resources (equal), Writing – original draft (supporting). M.E.: Writing – review and editing (supporting). M.G.: Resources (equal). O.H.H.: Writing – review and editing (supporting), Supervision (lead), Conceptualization (lead).

Declaration of Interests: The authors declare no conflicts of interest.

Statement: During the preparation of this work the authors used GPT-5 (OpenAI) in order to improve readability and clarity of the manuscript. After using this tool/service, the authors reviewed and edited the content as needed and take full responsibility for the content of the published article.

References

1. Djurišić, A., Li, E., Rakić, D. & Majewski, M. Modeling the optical properties of AlSb, GaSb, and InSb. *Applied Physics A: Materials Science & Processing* **70**, 29–32 (2000).
2. Bett, A. W. & Sulima, O. V. GaSb photovoltaic cells for applications in TPV generators. *Semiconductor Science and Technology* **18**, S184–S190 (2003).
3. Kwei-wei Huang, E., Haddadi, A., Chen, G., Hoang, A.-M. & Razeghi, M. Active and passive infrared imager based on short-wave and mid-wave type-II superlattice dual-band detectors. *Optics Letters* **38**, 22 (2013).
4. Cerutti, L. *et al.* GaSb-based VCSELs emitting in the mid-infrared wavelength range (2–3 μm) grown by MBE. *Journal of Crystal Growth* **311**, 1912–1916 (2009).

5. Zia, N., Viheriälä, J., Koivusalo, E. & Guina, M. High-power single mode GaSb-based 2 μm superluminescent diode with double-pass gain. *Applied Physics Letters* **115**, 231106 (2019).
6. Joullié, A. & Christol, P. GaSb-based mid-infrared 2–5 μm laser diodes. *Comptes Rendus. Physique* **4**, 621–637 (2003).
7. Yasuda, H., Sekine, N. & Hosako, I. Growth of InGaSb/AlInGaSb quantum cascade laser structures on GaSb substrates by molecular beam epitaxy. *Journal of Crystal Growth* **636**, 127720 (2024).
8. Gaulke, M. *et al.* Optically Pumped GaSb-Based Thin-Disk Laser Design Considerations for CW and Dual-Comb Operation at a Center Wavelength Around 2 μm . *IEEE Journal of Selected Topics in Quantum Electronics* **31**, 1–14 (2025).
9. Alaydin, B. Ö. *et al.* Bandgap engineering, monolithic growth, and operation parameters of GaSb-based SESAMs in the 2–2.4 μm range. *Optical Materials Express* **12**, 2382 (2022).
10. Schuchter, M. C. *et al.* Composition-controlled recovery time of SWIR (2–2.4 μm) GaSb-based SESAMs. *Optics Express* **33**, 14750 (2025).
11. Aspnes, D. E. & Studna, A. A. Dielectric functions and optical parameters of Si, Ge, GaP, GaAs, GaSb, InP, InAs, and InSb from 1.5 to 6.0 eV. *Physical Review B* **27**, 985–1009 (1983).
12. Muñoz Uribe, M. *et al.* Near-band-gap refractive index of GaSb. *Materials Science and Engineering: B* **38**, 259–262 (1996).
13. Ferrini, R., Patrini, M. & Franchi, S. Optical functions from 0.02 to 6 eV of $\text{Al}_x\text{Ga}_{1-x}\text{Sb}/\text{GaSb}$ epitaxial layers. *Journal of Applied Physics* **84**, 4517–4524 (1998).
14. Roux, S. *et al.* Mid-infrared characterization of refractive indices and propagation losses in GaSb/ $\text{Al}_x\text{Ga}_{1-x}\text{AsSb}$ waveguides. *Applied Physics Letters* **107**, 171901 (2015).
15. Wasiak, M., Motyka, M., Smołka, T., Ratajczak, J. & Jasik, A. Absorption and dispersion in undoped epitaxial GaSb layer. *Materials Research Express* **5**, 025907 (2018).
16. Adachi, S. Optical dispersion relations for GaP, GaAs, GaSb, InP, InAs, InSb, $\text{Al}_x\text{Ga}_{1-x}\text{As}$, and $\text{In}_{1-x}\text{Ga}_x\text{As}_y\text{P}_{1-y}$. *Journal of Applied Physics* **66**, 6030–6040 (1989).
17. Paskov, P. P. Refractive indices of InSb, InAs, GaSb, $\text{InAs}_x\text{Sb}_{1-x}$, and $\text{In}_{1-x}\text{Ga}_x\text{Sb}$: Effects of free carriers. *Journal of Applied Physics* **81**, 1890–1898 (1997).
18. Linnik, M. & Christou, A. Calculations of optical properties for quaternary III–V semiconductor alloys in the transparent region and above (0.2–4.0 eV). *Physica B: Condensed Matter* **318**, 140–161 (2002).
19. Fujiwara, H. *Spectroscopic ellipsometry: principles and applications* Printed with corrections (Wiley, Chichester, 2009).
20. Perner, L. W. *et al.* Simultaneous measurement of mid-infrared refractive indices in thin-film heterostructures: Methodology and results for GaAs/AlGaAs. *Physical Review Research* **5**, 033048 (2023).
21. Skauli, T. *et al.* Improved dispersion relations for GaAs and applications to nonlinear optics. *Journal of Applied Physics* **94**, 6447–6455 (2003).
22. Kim, C. C., Garland, J. W., Abad, H. & Raccah, P. M. Modeling the optical dielectric function of semiconductors: Extension of the critical-point parabolic-band approximation. *Physical Review B* **45**, 11749–11767 (1992).
23. Gaulke, M. *et al.* High average output power from a backside-cooled 2- μm InGaSb VECSEL with full gain characterization. *Optics Express* **29**, 40360 (2021).
24. Schuchter, M. C., Huwyler, N., Golling, M., Gaulke, M. & Keller, U. 2- μm 1.5-W Optically Pumped Semiconductor Membrane Laser. *IEEE Photonics Technology Letters* **36**, 543–546 (2024).
25. Huwyler, N. *et al.* 3-W output power from a 2- μm InGaSb VECSEL using a hybrid metal-semiconductor Bragg reflector. *Optical Materials Express* **13**, 833 (2023).
26. Lebigot, E. O. *Uncertainties: a Python package for calculations with uncertainties* 2024.
27. Newville, M. *et al.* *LMFIT: Non-Linear Least-Squares Minimization and Curve-Fitting for Python* 2025.
28. Luce, A., Mahdavi, A., Marquardt, F. & Wankerl, H. TMM-Fast, a transfer matrix computation package for multilayer thin-film optimization: tutorial. *Journal of the Optical Society of America A* **39**, 1007 (2022).
29. Terven, J., Cordova-Esparza, D.-M., Romero-González, J.-A., Ramírez-Pedraza, A. & Chávez-Urbiola, E. A. A comprehensive survey of loss functions and metrics in deep learning. *Artificial Intelligence Review* **58**, 195 (2025).
30. Lasdon, L., Duarte, A., Glover, F., Laguna, M. & Martí, R. Adaptive memory programming for constrained global optimization. *Computers & Operations Research* **37**, 1500–1509 (2010).
31. Nelder, J. A. & Mead, R. A Simplex Method for Function Minimization. *The Computer Journal* **7**, 308–313 (1965).

32. Gao, F. & Han, L. Implementing the Nelder-Mead simplex algorithm with adaptive parameters. *Computational Optimization and Applications* **51**, 259–277 (2012).
33. Alibert, C., Skouri, M., Joullie, A., Benouna, M. & Sadiq, S. Refractive indices of AlSb and GaSb-lattice-matched $\text{Al}_x\text{Ga}_{1-x}\text{As}_y\text{Sb}_{1-y}$ in the transparent wavelength region. *Journal of Applied Physics* **69**, 3208–3211 (1991).
34. Saleh, B. E. *Fundamentals of photonics* 2nd. ed. OCLC: 1378459105 (Wiley, New Delhi, 2018).